



Science Arts & Métiers (SAM)

is an open access repository that collects the work of Arts et Métiers Institute of Technology researchers and makes it freely available over the web where possible.

This is an author-deposited version published in: <https://sam.ensam.eu>
Handle ID: <http://hdl.handle.net/10985/19635>

To cite this version :

Zimo WANG, Pawan DIXIT, Behrouz TAKABI, Bruce L. TAI, Satish BUKKAPATNAM, Mohamed EL MANSORI, Faissal CHEGDANI - Bidirectional Gated Recurrent Deep Learning Neural Networks for Smart Acoustic Emission Sensing of Natural Fiber-Reinforced Polymer Composite Machining Process - Smart and Sustainable Manufacturing Systems - Vol. 4, n°2, p.179-198 - 2020

Any correspondence concerning this service should be sent to the repository

Administrator : scienceouverte@ensam.eu



Zimo Wang,¹ Pawan Dixit,^{2,3} Faissal Chegdani,^{2,4} Behrouz Takabi,⁵ Bruce L. Tai,⁵ Mohamed El Mansori,^{4,6} and Satish Bukkapatnam^{2,6}

Bidirectional Gated Recurrent Deep Learning Neural Networks for Smart Acoustic Emission Sensing of Natural Fiber-Reinforced Polymer Composite Machining Process

Reference

Z. Wang, P. Dixit, F. Chegdani, B. Takabi, B. L. Tai, M. El Mansori, and S. Bukkapatnam, "Bidirectional Gated Recurrent Deep Learning Neural Networks for Smart Acoustic Emission Sensing of Natural Fiber-Reinforced Polymer Composite Machining Process," *Smart and Sustainable Manufacturing Systems* 4, no. 2 (2020): 179–198. <https://doi.org/10.1520/SSMS20190042>

ABSTRACT

Natural fiber-reinforced polymer (NFRP) composites are increasingly considered in the industry for creating environmentally benign product alternatives. The complex structure of the fibers and their random distribution within the matrix basis impede the machinability of NFRP composites as well as the resulting product quality. This article investigates a smart process monitoring approach that employs acoustic emission (AE)—elastic waves sourced from various plastic deformation and fracture mechanisms—to characterize the variations in the NFRP machining process. The state-of-the-art analytic tools are incapable of handling the transient dynamic patterns with long-term correlations and bursts in AE and how process conditions and the underlying material removal mechanisms affect these patterns. To address this gap, we investigated two types of the bidirectional gated recurrent deep learning neural network (BD-GRNN) models, viz., bidirectional long short-term memory and bidirectional gated recurrent unit to predict the process conditions based on dynamic AE patterns. The models are tested on the AE signals gathered from orthogonal cutting experiments on NFRP samples performed at six different cutting speeds and three fiber orientations. The results from the experimental study suggest that BD-GRNNs can correctly predict (around 87 % accuracy) the cutting conditions based on the extracted temporal-spectral features of AE signals.

¹ Department of Industrial and Systems Engineering, Texas A&M University, 3131 TAMU, College Station, TX 77843, USA
(Corresponding author), e-mail: zimo.zmw@gmail.com, <https://orcid.org/0000-0001-9667-0313>

² Department of Industrial and Systems Engineering, Texas A&M University, 3131 TAMU, College Station, TX 77843, USA

³ Capital One Financial Corp, Richmond, VA, USA

⁴ Arts et Metiers Institute of Technology, MSMP, HESAM Université, Châlons-en-Champagne, F-51006, France

⁵ Texas A&M University, Department of Mechanical Engineering, 3123 TAMU, College Station, TX 77843, USA

⁶ Texas Engineering Experiment Station, Institute for Manufacturing Systems, College Station, TX 77843, USA

Keywords

smart sensing, deep learning approaches, natural fiber–reinforced composites

Introduction

Because of recent moves toward sustainable manufacturing, natural fiber–reinforced polymer (NFRP) composites are becoming increasingly attractive for various industrial applications, such as for panels, window frames, and decking for industries such as automotive, construction, and aerospace companies.¹ NFRPs offer an attractive balance between cost, carbon footprint, and performance. The applications of NFRP have widely expanded through the last few years, and the NFRP industry sector has reached \$2.1 billion (USD) in the 2010s with a 10% growing rate worldwide.²

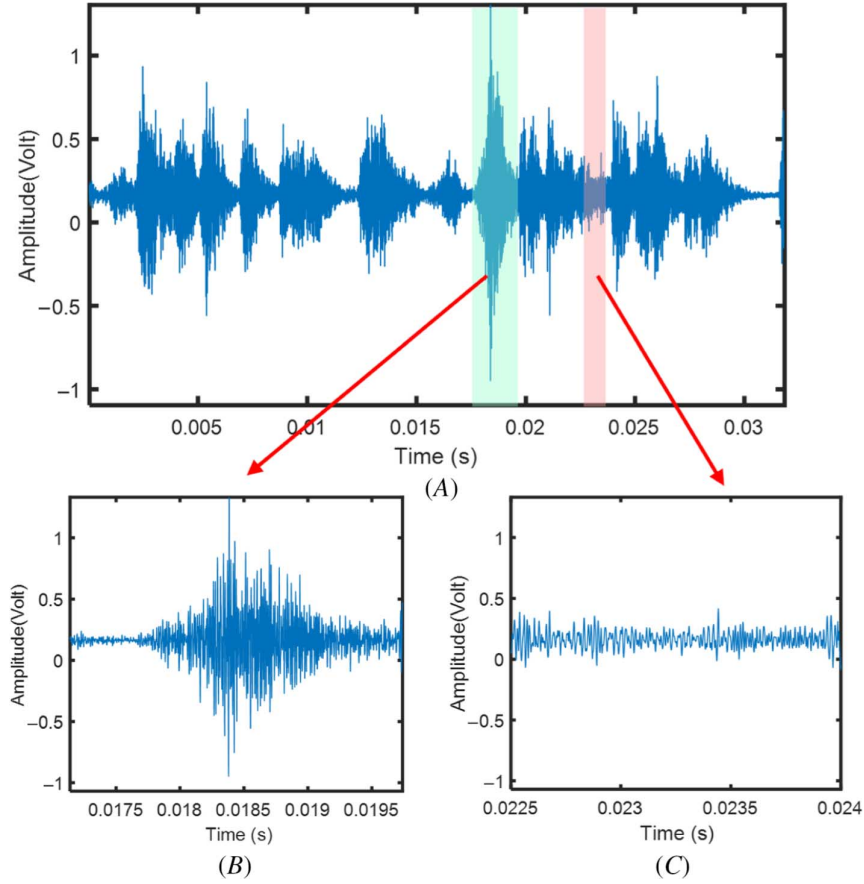
Most of the emerging industrial applications necessitate machining of these NFRP composite panels to dimensional tolerances of ± 1 mm and surface roughness within 1 μm . Currently, machining process is crucial for realizing NFRPs' functionality as the machined surface quality is highly related to the bearing of mechanical property of the NFRP products. However, NFRPs possess complex material characteristics, such as viscoelastic behaviors and thermal effect.³ In particular, their complex multiscale structure poses significant challenges for machining. Because of the natural fibers' cellulose structure and their orientations in the composites, these randomly distributed elementary/bundle fibers within the matrix basis introduce distinct material removal mechanisms, create surface conformity issues, and consequently influence the overall machinability of such a material for industrial applications.

Current investigations into characterizations of the NFRP machining processes heavily rely on offline approaches (e.g., mechanical property testing and imaging instruments^{4,5}). Though these methods are powerful in measuring the finished surface morphology and characterizing various modes of material removal, they cannot capture the effects of the heterogeneity and the fibers' distribution over the multiple scales of the matrix on material removal mechanisms. In addition, such offline tools are impractical for in-process monitoring of the NFRP machining processes. Therefore, a real-time sensing approach is desirable to characterize machining processes, evaluate machined surface quality, and provide timely intervention for in-process quality assurance.⁶ Among various sensor candidates, the acoustic emission (AE) sensor shows potential for in-process monitoring of the cutting processes at the precision level (depth of cut within 10s of micrometers). The AE waves gathered during the machining process are sourced from the (elasto)plastic deformation, fracture, and friction at interfaces between the cutting tool, workpiece, and chips from machining processes.^{7–9} In addition, AE waveforms are also related to the crack formation and chip breakage, entanglement, or both during the material removal process. However, such elastic transient waves during machining processes may be highly affected by the environmental noises, and consequently, they have a low signal-to-noise ratio. The challenge remains as to how to analyze such nonstationary signals with strong transient behaviors.

Most representative time portraits of the AE's transient patterns are listed in [figure 1](#)—[figure 1A](#) depicts a burst-patterned AE waveform, which oftentimes contains higher frequency responses with sharp rising and decaying times, and [figure 1B](#) shows a near-stationary (also referred to as “continuous”) AE signal with low energy and long decaying time.¹⁰ During an NFRP cutting process, fast-streamed AE data may exhibit both types of behavior: continuous waveforms combined with (irregular) intermittent bursts. Each of the waveform patterns may be due to the energy released from a distinct material removal mechanism. Therefore, the prominent moves toward analyzing the AE waveforms may be related to how to connect the short time-dependent waveform patterns (intermittent bursts and resultant time-varying frequency responses) with different cutting conditions that result in changes of the fundamental cutting mechanisms.

From the perspective of the dynamic system, this transient behavior is referred to as dynamic intermittency.¹¹ The transitions between intermittent bursts and laminar phases from such a system create nonstationarity with time-variant dependency. Thus far, analyzing the intermittent AE signals is still challenging. Chang and Bukkapatnam¹² and Bukkapatnam and Chang¹³ investigated the AE sensor signal's connection to microdynamics for machining metallic materials. Results suggest that the energy of AE signals sourced from the plastic deformation

FIG. 1 (A) A representative AE waveform showing two distinct characteristics: (B) AE bursts and (C) stationary emission.¹⁰



is related to the shear strain and shear strain rate. The stress releases that are due to the grain dislocation during the material removal processes may result in such time-varying intermittency patterns in AE waveforms.¹⁴ Intuitively speaking, how to treat transient intermittent AE events is akin to how a human brain recognizes/ processes the information in speeches or music clips. Currently, deep learning approaches and hidden Markov models¹⁵ have been selected as powerful tools for processing acoustic signals. Such approaches apply windows with fixed sizes to investigate contextual information from neighboring windows/frames to process the time-varying signals and improve training accuracy. However, the optimal length for preserving the contextual information in AE signals may be varied case by case because of its time-varying nature, suggesting that conventional deep learning algorithms or hidden Markov models may not be sufficient to explore the time-variant nature of the AE signal. Researchers have also presented recurrent neural networks (RNNs) for investigating the time-varying nature of streaming/sequential data, such as acoustic recognition problems.¹⁶ Kamarthi, Kumara, and Cohen,¹⁷ and Pittner Kamarthi, and Gao,¹⁸ and Pittner and Kamarthi¹⁹ presented a wavelet-based neural network that extracts the spectral features in a multisensor setup for detecting cutting tool wears. Comparatively, RNNs containing cyclic connections are regarded as more powerful tools to model the nonstationary transient data, especially time-varying acoustic signals.^{20,21} The RNN encodes the sequential data in the internal states and allows an estimation of the following steps based on all previous information up to the current time point. Hence, RNNs have demonstrated the success in sequence labeling and prediction tasks in nonstationary real-world processes, such as handwriting recognition and language modeling.²² However, conventional RNNs may be difficult to train and can merely model short time-dependent effects (the intermittent bursts

in AE signals are both long and short time dependent). Toward overcoming this drawback, an RNN framework²³ that uses fractal properties of the attractor of the underlying dynamic system along with other machining parameters as the training inputs was developed to predict flank wear in machining. Furthermore, a recurrent predictor neural network²⁴ was applied to capture the evolution of complex nonlinear and nonstationary processes (e.g., real-time sensor signals) and detect the incipient surface deterioration in ultraprecision machining (UPM) processes. Cheng et al.²⁵ applied a Gaussian process with extracted statistical features as well as features extracted based on nonlinear recurrent analysis for real-time prediction of the achieved surface characteristics during UPM. Kannatey-Asibu and Dornfeld^{26,27} presented statistical analytic approaches to analyze AE signals for monitoring the cutting tool condition and related the AE features to the metal-cutting process parameters. A nonparametric approach from our earlier effort²⁸ was presented to model the transient behaviors of nonstationary sensor signals during machining processes.

In this article, we present a sensor-based monitoring approach for smart sensing and AE characterizations for machining NFRPs. To address this gap, we investigate the gated recurrent neural network (GRNN) models to relate the AE waveform features to different process conditions and the underlying material removal mechanisms of machining NFRPs. During the orthogonal cutting experiments, AE signals were gathered from the testbed equipped with a multisensor data acquisition system. To connect the AE signal patterns to the machining mechanisms of NFRP cutting, we employ GRNN models for characterizing the temporal-spectral features of AE signals. The rest of this article is organized as follows: the framework of the presented approach is introduced in “Overview of Recurrent Deep Learning Approaches.” The experiment details about the orthogonal cutting experimental setup, implementation of GRNN models, and results for AE characterizations are presented in “Temporal-Spectral Features-based GRNN for AE Characterizations.” Concluding remarks are provided in “Summary and Concluding Remarks.”

Overview of Recurrent Deep Learning Approaches

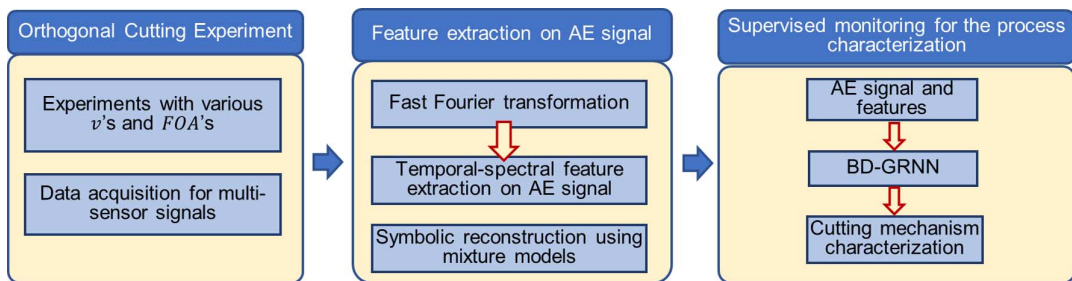
We present the framework of GRNN for characterizations of AE signals gathered from orthogonal cutting experiments. **Figure 2** summarizes the schematic diagram for implementing GRNNs. During the orthogonal cutting experiment, sensor signals were recorded with various cutting conditions (varying cutting speeds (v) and fiber orientation angles (FOA)). The temporal-spectral features were extracted using a sliding-windowed time-frequency analysis over specified microseconds-long time windows. To handle the time-varying frequency response of the AE signal and relate it to different machining conditions during NFRP cutting, the temporal-spectral features are directly treated as the input series in the GRNN for characterizing the cutting processes. Therefore, ad-hoc feature selection and extraction are avoided. The GRNNs were then developed for training and prediction/estimations on characterizing the time-spectral features of AE waveforms.

GENERAL STRUCTURE OF LONG SHORT-TERM MEMORY AND GATED RECURRENT UNIT

The general RNN can be presented as follows:

$$h_t = \mathcal{H}(W_{xh}x_t + W_{hh}h_{t-1} + b_h) \quad (1)$$

FIG. 2 Schematic diagram of the presented research approach.



$$y_t = W_{hy}h_t + b_y \quad (2)$$

where x_t , y_t , and h_t are the input, output, and hidden state, respectively. The matrix W s are weight matrices (e.g., W_{xh} is the weight matrix for the layer connecting the inputs and the hidden nodes, W_{hh} is the weight matrix between hidden layers, and W_{hy} is the weight matrix between the hidden layer and output layer). \mathcal{H} is the hidden layer function, and the b 's are the bias vectors (b_h is the hidden bias vector and b_y is the output bias vector). To extend the formula to the GRNN, two models, namely long short-term memory (LSTM) cell and gated recurrent unit (GRU), are introduced. The LSTM uses the input, forget, and output gates, and the GRU model uses the reset and update gated units. Both LSTM and GRU apply these gated units to track time-dependent recurrence relations while mitigating the issues of vanishing or exploding gradient problems or both.²⁹ In this article, we developed both LSTM and GRU-based approaches for constructing the GRNN to capture the transient nature of AE, and based on the comparisons between two presented GRNN approaches using numerical and experimental case studies, we further applied the optimal model for characterizations of AE signals during the machining processes on the NFRPs. The details of these two models are described in the following subsections.

LSTM Cell

As mentioned, LSTM considers the dependencies on previous states at different timescales by applying input, forget, and output gates. This feature may help capture the intermittent transient data with time-variant long-short time dependencies. One can formulate the structure of the LSTM cell as follows:

$$i_t = \sigma(W_{xi}x_t + W_{hi}h_{t-1} + W_{ci}c_{t-1} + b_i) \quad (3)$$

$$f_t = \sigma(W_{xf}x_t + W_{hf}h_{t-1} + W_{cf}c_{t-1} + b_f) \quad (4)$$

$$c_t = f_t c_{t-1} + i_t \tanh(W_{xc}x_t + W_{hc}h_{t-1} + b_c) \quad (5)$$

$$o_t = \sigma(W_{xo}x_t + W_{ho}h_{t-1} + W_{co}c_t + b_o) \quad (6)$$

$$h_t = o_t \tanh(c_t) \quad (7)$$

where σ is the activation function (which is often selected as the logistic sigmoid function) and i, f, o , and c are, respectively, the input gate, forget gate, output gate, and cell activation vectors (with the same size as the hidden vector h). The matrix W s are the weight parameters for different memory cells: W_{xi} is the weight matrix for the input gate, W_{hi} is the matrix connecting hidden layer and the input gate, and W_{ci} connects the cell activation and the input gate. W_{xf} , W_{hf} , and W_{cf} are the matrices connecting the inputs, hidden layers, and activation vector to the forget gate, and similarly, W_{xo} , W_{ho} , and W_{co} are the matrices connecting the inputs, hidden layers, and activation vector to the output gate. The b 's are the bias vectors (e.g., b_i is the input gate bias vector and b_f is the forget gate bias vector).

GRU

Compared with the LSTM cell, the general GRU unit does not possess a separated memory (c_t) or the output gate. Instead, it applies recurrent reset and update units for capturing the time-dependent features at different time scales.²⁹ A general GRU can be formulated as follows:

$$z_t = \sigma(W_{xz}x_t + W_{hz}h_{t-1} + b_z) \quad (8)$$

$$r_t = \sigma(W_{xr}x_t + W_{hr}h_{t-1} + b_r) \quad (9)$$

$$\tilde{h}_t = \tanh(W_{x\tilde{h}}x_t + W_{r\tilde{h}}(r_t \circ h_{t-1}) + b_{\tilde{h}}) \quad (10)$$

$$h_t = (1 - z_t)h_{t-1} + z_t\tilde{h}_t \quad (11)$$

where z_t and r_t are, respectively, the update gate and reset gate vectors; the activation h_t at time t is a linear interpolation between the previous activation h_{t-1} and the candidate activation \tilde{h}_t ; the b 's are the bias vectors for different cells (b_z, b_r , and $b_{\tilde{h}}$ are the bias terms for the update gate, the reset gate, and the candidate activation, \tilde{h} , respectively); W s are the weight matrices (e.g., W_{xz} is the matrix between the inputs x and the update gate z); and the activation function σ is chosen with the sigmoid kernel. The operator \circ denotes a Hadamard product.

Bidirectional LSTM and GRU

As one drawback of the RNNs, they only consider the previous information for inferencing the system outputs; the bidirectional (BD)-GRNN is applied to characterize the AE signal with the transient nature by considering the forward and backward states for inferencing the transient burst and jumps between sojourns/stationary segments. In general, the BD-GRNN contains two sets of layers (one for forward information and the other for the backward direction as shown [fig. 3](#)). One can extend the formulas to a BD-GRNN as follows:

$$\vec{h}_t = \mathcal{H}(W_{xh} \vec{x}_t + W_{h\vec{h}} \vec{h}_{t-1} + b_{\vec{h}}) \quad (12)$$

$$\overleftarrow{h}_t = \mathcal{H}(W_{x\overleftarrow{h}} \vec{x}_t + W_{\overleftarrow{h}h} \overleftarrow{h}_{t-1} + b_{\overleftarrow{h}}) \quad (13)$$

$$y_t = W_{hy} \vec{h}_t + W_{h\overleftarrow{y}} \overleftarrow{h}_t + b_y \quad (14)$$

The BD-GRNN contains the forward hidden sequence \vec{h} , the backward hidden sequence \overleftarrow{h} , and the output sequence y . The matrix W s are different weights for the associated layers (e.g., W_{xh} connects the inputs x and the forward hidden layer \vec{h}). $b_{\vec{h}}$, $b_{\overleftarrow{h}}$, and b_y are the bias vectors for the forward hidden layer, backward hidden layer, and output layer, respectively.

As suggested by the schematic diagrams of LSTM and GRU in [figures 4](#) and [5](#), it may be noted that, compared with the conventional RNN, the gate units in LSTM and GRU (e.g., the memory cell of the LSTM and the update/reset gate of the GRU) keep the present states and add the new content on top, which in turn constructs the recurrent relations (similar to the iterative map for modeling the nonstationary dynamic systems). Such a scheme provides a prominent feature toward capturing the transient behaviors of the input data.

FIG. 3

Schematic diagram of a BD-GRNN neural network where each box represents a gated unit.

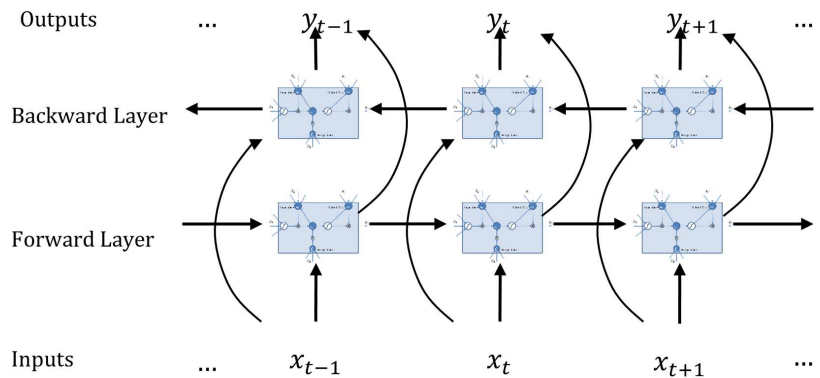


FIG. 4

Schematic diagram showing the structure of an LSTM cell.³⁶

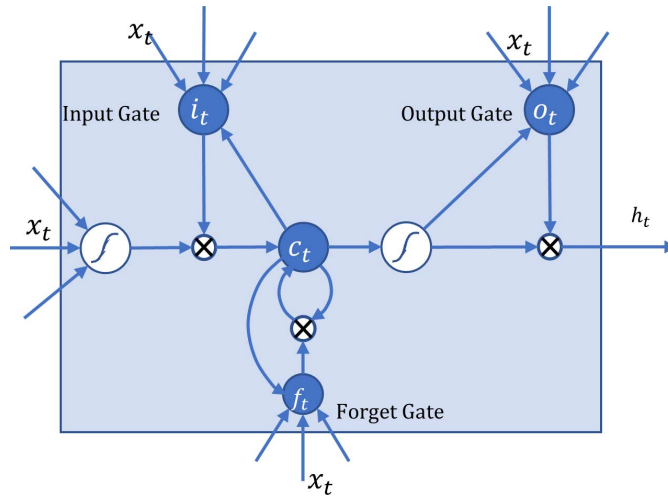
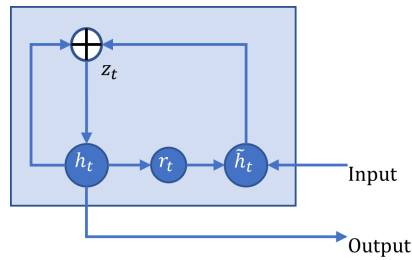


FIG. 5

Schematic diagram showing the structure of a GRU unit.

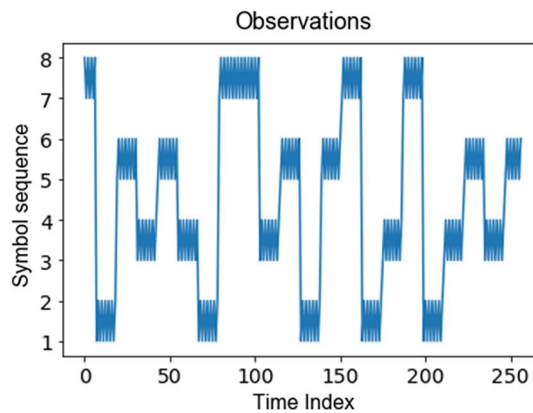


CAPTURING TRANSIENT BEHAVIORS USING LSTM AND GRU

To demonstrate the capability of the presented approach for characterizations of transient processes, an illustrative example based on the chord progression of the major pentatonic scale is presented. As noted earlier, such a chord progression follows intermittent dynamics²⁸ and is therefore well suited to illustrate the performance of our approach. **Figure 6** shows a representative snippet of the symbolic sequence of chord progressions.

FIG. 6

Plot of the symbolic sequence showing the tokenized chord progressions. Each chord is encoded with a unique number, i.e., {1: B, 2: E, 3: B^b, 4: F, 5: A, 6: D, 7: G, 8: C}.



Here, the vertical axis represents different chords, and the horizontal axis is the time index referring to the number of the music note. Each chord is tokenized with a unique number, viz., number 1 mapping to the note B, 2 mapping to the note E, 3 to B^b, 4 to F, 5 to A, 6 to D, 7 to G, and 8 to C. There are four types of chords considered here: C-G, D-A, E-B, and F-B^b. Each segment (referred to as a pentatonic note progression) lasts for 3 bars under the 4/4 time signature (i.e., 12 data points). After this duration, the note is transitioned as determined by a Markov transition matrix given by the following:

$$A = \begin{bmatrix} 0.051 & 0.128 & 0.179 & 0.641 \\ 0.459 & 0.030 & 0.060 & 0.451 \\ 0.385 & 0.051 & 0.051 & 0.513 \\ 0.135 & 0.270 & 0.541 & 0.054 \end{bmatrix}$$

Here, each row corresponds to the original pentatonic chord progression (e.g., first element for the pentatonic chord of C-G, the second for D-A, the third to E-B, and the fourth to F-B^b), and each column contains the destination pentatonic chords.

The implemented model has two layers of the gated units for both forward and backward directions with a detailed structure as plotted in [figure 7B](#). Each layer is set with neuron nodes as 100, the batch size is set as 40, and the training epoch is selected around 30 to ensure that the loss function value during training converges to its minimal. The prediction performance on the trained BD-LSTM as well as BD-GRU is tested on simulated chord progressions.

The results of BD-LSTM for one-step and five-step look-ahead predictions (i.e., forecasts) are correspondingly shown in [figure 8A](#) and [8C](#). In comparison, [figure 8B](#) and [8D](#) includes the prediction results from BD-GRU for one and five-step forecasting. The observations (symbolic sequence) are plotted using solid lines, while the lines with triangles represent the estimated sequences. Remarkably, as illustrated in the magnified block (dashed outline) in [figure 8](#), the BD-GRNN model is able to capture the transitions between scales as it accurately predicts the jumps among multiple sojourns (in-between segments of the chord progressions). It is evident that both one-step and five-step predictions for both BD-LSTM and BD-GRU models possess high accuracies demonstrated by nearly 100 % for the R^2 values as shown in [Table 1](#).

From the numerical case study, one can conclude that the developed BD-GRNNs can properly capture the complicated recurrence relations between states. The transient AE signals may exhibit similar recurrent patterns, which combine irregular bursts and stationary segments caused by the material fracture and intermittent dislocations during machining. Hence, the presented approaches have prominent application merits toward

FIG. 7 (A) A schematic diagram for the structure of input variables, (B) the hierarchical structure of the bidirectional neural network, and (C) the losses with training and cross validation.

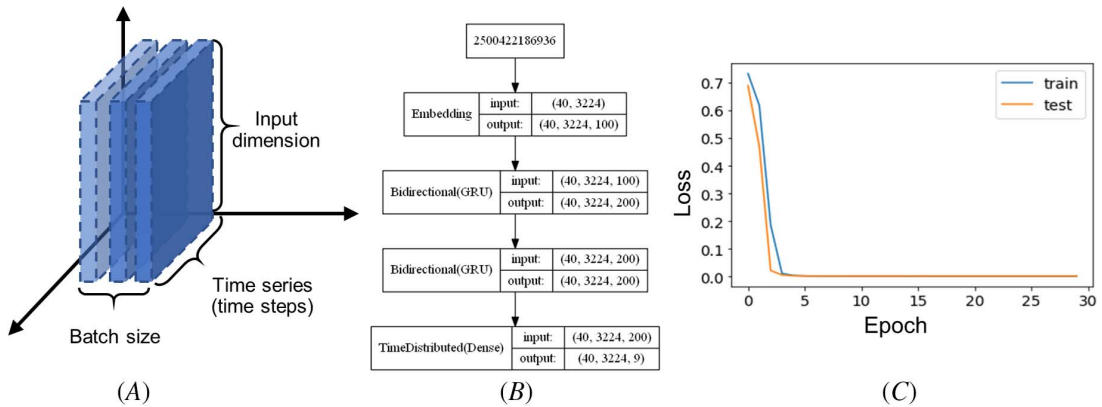


FIG. 8 Result comparisons of one and five-step ahead predictions, where (A) and (C) are generated from BD-LSTM and (B) and (D) list the results from the BD-GRU model. Here, the predicted sequences are plotted as dashed lines with triangle markers, the ground truth is shown using the solid lines, and the inset (dashed rectangle) magnifies a short, 10 data point snippet of the prediction result. Both one-step ((A) BD-LSTM vs. (B) BD-GRU) and five-step ((C) BD-LSTM vs. (D) BD-GRU) predictions suggest that two developed models can finely capture the jumps between stationary segments of the chord progression transitions.

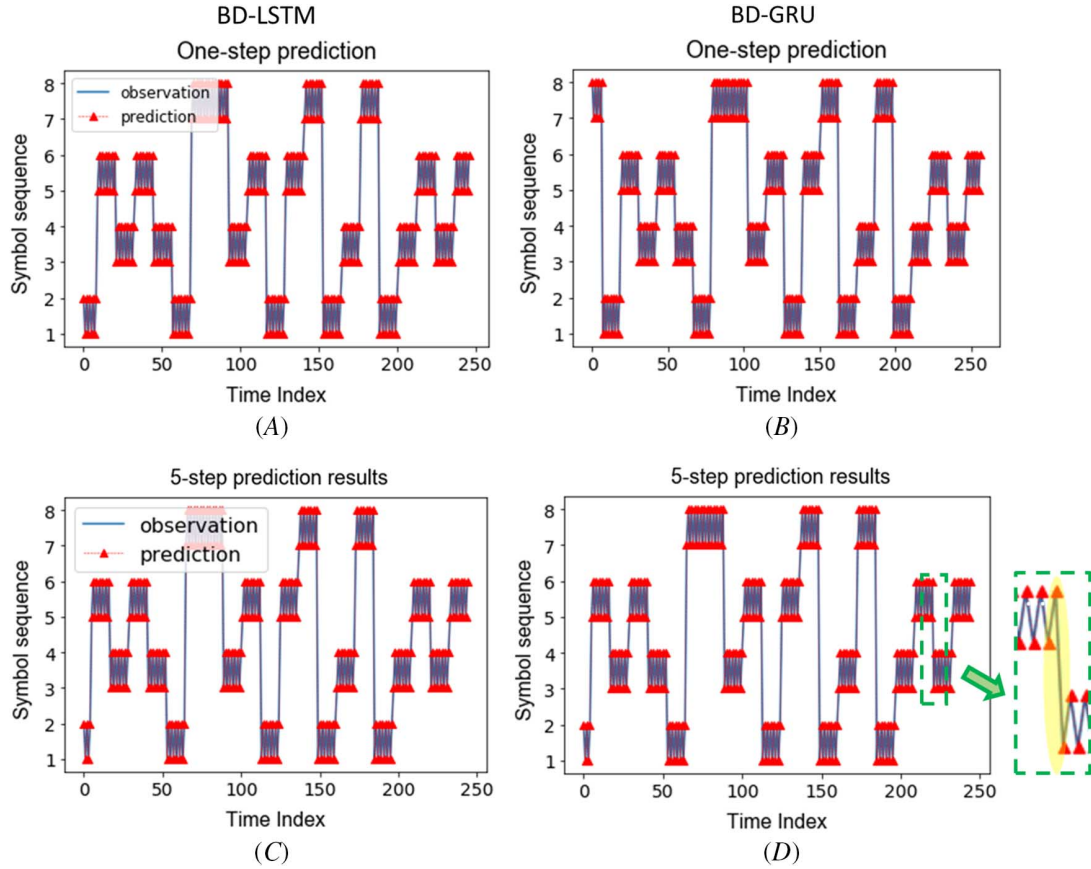


TABLE 1

Accuracy for symbolic sequence prediction

R^2	One Step	Five Steps
BD-LSTM	0.99	0.99
BD-GRU	0.99	0.99

capturing the intermittent AE waveform signals for monitoring machining process: as the model trains the gates to construct the recurrence relations using the sequential data, it captures the transient behaviors of the AE signals under different machining conditions. To test the presented approach toward smart sensing for AE characterizations, an experimental case study on machining NFRP processes was further investigated. Details on the experiment setup as well as the case study results are presented in the following sections.

Temporal-Spectral Features-based GRNN for AE Characterizations

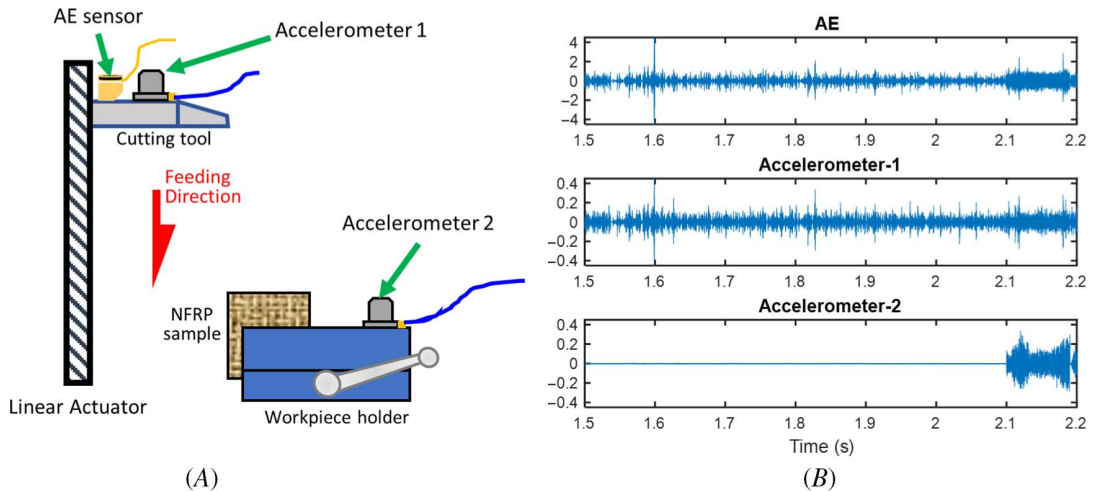
EXPERIMENTAL SETUP

Multiple sets of experiments were conducted on an orthogonal cutting testbed, as shown in the schematic diagram in [figure 9](#). The orthogonal cutting setup consists of two linear sliders and a workpiece clamping vice. The cutting tool setup, consisting of a polycrystalline diamond cutting tool insert (Sandvik Coromant model TCMW16T304FLP-CD10) and a tungsten carbide substrate, was attached to one linear actuator (L70, Moog Animatics, Milpitas, CA). A high-torque servomotor drives the linear actuator to ensure a consistent cutting feed rate. During the orthogonal cutting experiments, two accelerometers (Kistler Type 8728A500) were allocated on the tool holder (as Accelerometer 1) and the workpiece clamping vice (Accelerometer 2) separately for gathering the vibration signals, while an AE sensor (Physical Acoustics S9225) was mounted next to the Accelerometer 1 on the cutting tool holder for collecting AE signal during the orthogonal cutting processes. The data acquisition system (National Instruments CompactDAQ with DAQ Module NI-9223) is applied to rapidly stream the sensor data at 1 MHz sampling rate for each channel. The workpiece samples and mounted on clamp-on vice used the unidirectional flax fiber-reinforced polypropylene composites (manufactured by the material supplier Composites Evolution (UK)). Each NFRP workpiece (with dimensions as 20 by 15 by 4 mm³) has fiber volume fraction around 40 % and polyester weft fiber, which helps maintain the unidirectionality of the natural fiber, around 5 %. The orthogonal cutting experiments were conducted with the depth of cut $\sim 10 \mu\text{m}$ at different cutting conditions with varying cutting speeds ($v = 2, 4, 6, 8, 10, 12 \text{ m/min}$) and different FOAs ($\text{FOA} = 0^\circ, 45^\circ, \text{ and } 90^\circ$) toward the cutting direction.

TEMPORAL-SPECTRAL FEATURE EXTRACTION

A set of the representative sensor signals synchronously collected from the two accelerometers (separately mounted on the tool holder and the workpiece holder) and the AE sensor (on the tool holder) is shown in [figure 9B](#). It may be noted that Accelerometer 2 (attached to the workpiece holder) can properly separate the dynamics of the cutting and noncutting stages because of its sudden increase in amplitude when the cutting initiates. This allows us to isolate the signals of the cutting and noncutting stages.

FIG. 9 Schematic diagram showing the experimental setup: (A) the orthogonal cutting process with mounted AE and vibration sensors, and (B) the collected signals from the AE sensor and two vibration sensors during an orthogonal cutting experiment ($\text{FOA} = 0^\circ$ and $v = 4 \text{ m/min}$).



The AE signal captures the transients, i.e., time-varying frequency patterns associated with the material deformations, fractures, or both that occur at irregular intervals during machining.³⁰ To further process the AE signals, the temporal-spectral features are then extracted. Such time-frequency features could be visually represented using a spectrogram, as shown in **figure 10B**, where the x axis represents the time index, the y axis is the frequency range, and a colormap is applied to represent the strength of the frequency component. Such a spectrogram records the frequency components of the signal and their variations over time. The following procedures summarize the generation of the temporal-spectral features:

1. A sliding window with window width $L = 125$ is applied to collect a set of AE signals at the time index t , i.e., $\{x_{t-L+1}, x_{t-L+2}, \dots, x_t\}$.
2. Then, the fast Fourier transformation (FFT) is applied to compute the frequency component:

$$X_k^{(t)} = \sum_{n=t-L+1}^t x_n e^{-\frac{j2\pi kn}{L}} \quad k = 0, 1, \dots, L-1 \quad (15)$$

where $\{x_n\}$ (for $n = t-L+1, t-L+2, \dots, t$) is the time series of the AE signal within the sliding window L , and the FFT generates the frequency components $\mathbf{X}^{(t)} = [X_1^{(t)}, X_2^{(t)}, \dots, X_L^{(t)}]^\top$. By sequentially generating the frequency component vectors $\mathbf{X}^{(t)}$ (for $t = L, L+1, L+2, \dots, T$, where T is the time stamp at the end of the data recording), the matrix of the spectrogram could be represented as $M_{TF} = [\mathbf{X}^{(L)}, \mathbf{X}^{(L+\theta)}, \mathbf{X}^{(L+2\theta)}, \dots, \mathbf{X}^{(T)}]$, where θ denotes the step of the sliding window.

Figure 11A–C shows the spectrograms of the AE and two vibration signals, capturing the temporal-spectral features of the tool-approaching and cutting phases. The spectrograms as shown in **figure 11** were generated by the FFT with a sliding window of 0.125 ms and a 50 % time step (i.e., $\theta = 0.5 L$). This translates to a temporal resolution of 0.125 ms (x axis), and we select 200 Hz as the spectral resolution (y axis). The edge effect that is due to the sliding window may be ignored, as the window size (0.125 ms duration) is smaller than the durations

FIG. 10 (A) The time portraits show the synchronized AE signal along with vibration signals from the tool holder (Accelerometer 1) and the workpiece holder (Accelerometer 2) during an orthogonal cutting process experiment; (B) and (C) show the temporal-spectral feature extraction. Machining condition: $FOA = 0^\circ$ and $v = 4$ m/min.

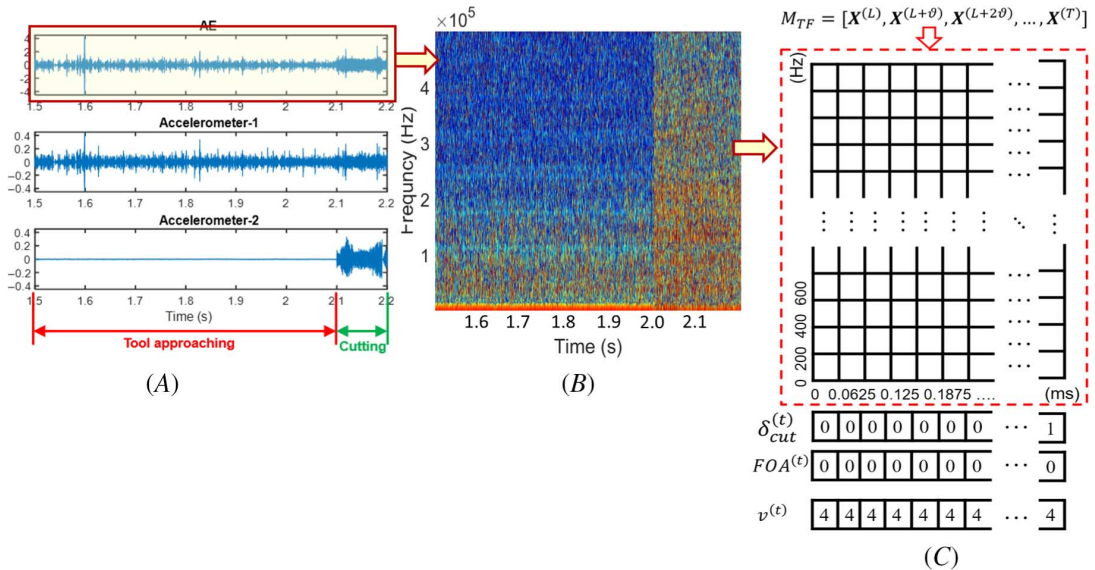
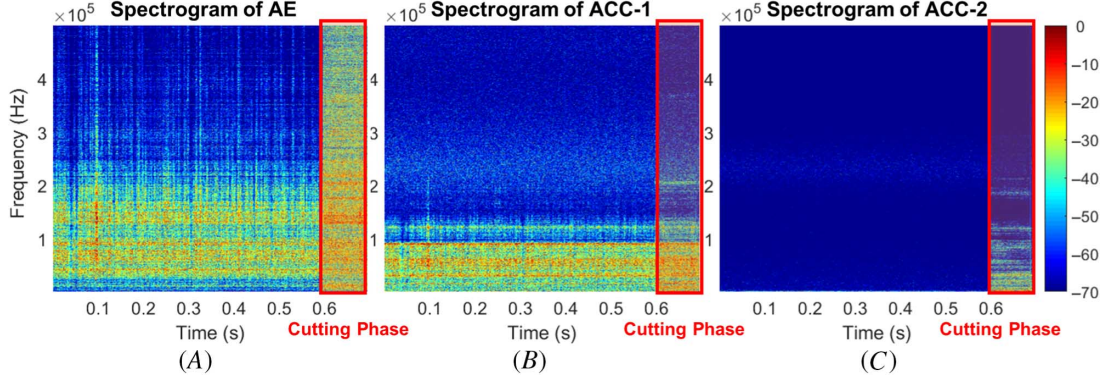


FIG. 11 Representative time-frequency domain spectrograms gathered during an orthogonal cutting experiment ($v=8$ m/min, FOA as 45°): (A) AE sensor, (B) Accelerometer 1 (ACC-1), and (C) Accelerometer 2 (ACC-2). Here, the rectangular frames at the right side of every plot indicate the temporal-spectral information during the cutting phase.



of the overall recordings (which normally last for seconds) by 4~5 orders of magnitude. The dimension of the temporal-spectral features is then illustrated in [figure 10](#). Each element in the spectrogram matrix represents the energy, ranging from -70 dB to 0 dB. The sensitivity of the AE sensor can be validated by the high-frequency response of the AE signal ([fig. 11A](#)) compared with the vibration signals shown in [figure 11B](#) and [11C](#).

Note that the multisensor setup segments the cutting and noncutting phases for the time-frequency features. Let τ_1 and τ_2 be the start and end time stamps of the segment for the cutting phase (e.g., the start and end points of the rectangular frame shown in [fig. 11A](#)). The response vector \mathbf{Y} , during the cutting phase, contains the control parameters for the designed experiments, i.e., $\mathbf{Y}^{(t)} = [FOA^{(t)}, v^{(t)}]^T$ for $t = \tau_1 + L, \tau_1 + L + \vartheta, \tau_1 + L + 2\vartheta \dots, \min(T, \tau_2)$, where $FOA \in \{0^\circ, 45^\circ, 90^\circ\}$ and cutting speed $v \in \{2, 4, 6, 8, 10, 12\}$ (m/min). Given the time duration T_0 (in seconds) of the recording, let $T = T_0 \times Fs$, where Fs is the sampling rate ($Fs = 1$ MHz for all experiment recordings). Then, the extracted features \mathbf{X} as well as the process responses \mathbf{Y} for a single recording Ω could be represented in the following format:

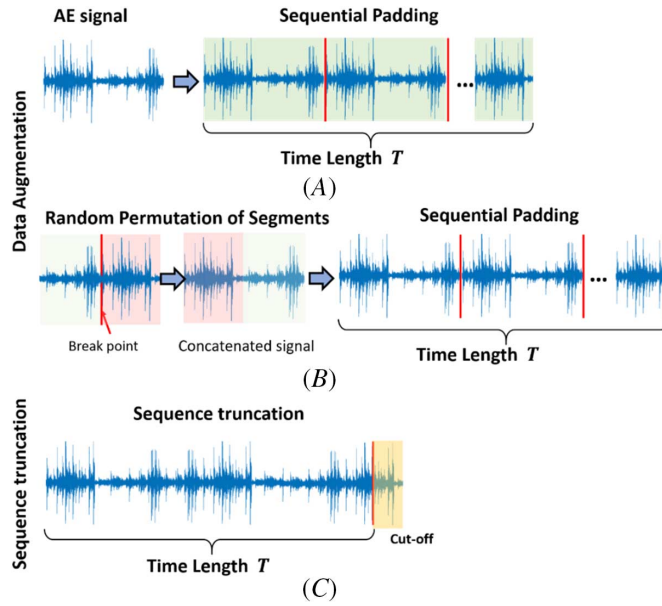
$$\Omega = [\mathbf{X}^{(t)T}, \mathbf{Y}^{(t)T}]^T = \begin{bmatrix} \mathbf{X}^{(L)} & \mathbf{X}^{(L+\vartheta)} & \mathbf{X}^{(L+2\vartheta)} & \dots & \mathbf{X}^{(T)} \\ \mathbf{Y}^{(L)} & \mathbf{Y}^{(L+\vartheta)} & \mathbf{Y}^{(L+2\vartheta)} & \dots & \mathbf{Y}^{(T)} \end{bmatrix} \quad (16)$$

The GRNN model is applied to capture the empirical relationships of the AE spectral features $\{\mathbf{X}^{(t)}\}$ with $\{y^{(t)}\}$, where $y^{(t)}$ is a subset of the response $\{\mathbf{Y}^{(t)}\}$ (e.g., $y^{(t)} = FOA^{(t)}$ for the classification of fiber orientations). To create the GRNN models,³¹ data augmentation is needed to ensure that all the input sequences for both training and testing data have the same lengths. One straightforward method is to repeat the temporal-spectral feature data $\{\mathbf{X}^{(t)}\}$ and responses $\{y^{(t)}\}$ in the testing data set until the length of $\{\mathbf{X}^{(t)}\}$ in the testing set is equal to $\{\mathbf{X}^{(t)}\}$ in the training set. In total, 38 experiments (90° with 1 single repetition for each cutting speed) were conducted with different fiber orientations and cutting speeds.

To ensure the training and testing datasets for each set of parameters have the same data length (as required by the GRNN models), we apply the data augmentation³² to keep the duration as 250 ms for each cutting experiment. Because of the variations in the cutting speeds, the durations of the cut and the associated lengths of the signal recordings vary from ~ 30 to ~ 260 ms. Hence, for the conditions with higher cutting speeds (shorter time durations), the signals are sequentially padded (as illustrated in [fig. 12A](#)) to maintain the data length as 250 ms.

FIG. 12

A schematic diagram showing the data augmentation schemes for AE signals: (A) sequential padding, (B) random permutation followed by sequential padding, and (C) sequence truncation.



Recordings with lower speeds (longer durations), on the other hand, are truncated (see [fig. 12C](#)) to keep the recording length as 250 ms. For those conditions with one repetition, samples have been randomly permuted (as shown in [fig. 12B](#)) followed by sequential padding to avoid the exact same data/signals utilized in both training and testing datasets, hence reducing the chance of overfitting.

BD-LSTM AND BD-GRU FOR MONITORING CUTTING CONDITION VARIATIONS WITH RESPECT TO FIBER ORIENTATIONS

Given the extracted time-frequency features $\{X^{(t)}\}$ and the response $\{y^{(t)}\} = \{FOA^{(t)}\}$, the BD-LSTM and GRU models are applied for classifying the cutting conditions. The details of the structure of the BD-LSTM and BD-GRU are described as follows.

The input for the extracted temporal-spectral features is with the dimension as $T \times 2,499$, where T is the length/duration of the temporal-spectral data with 2,499 rows of the frequency component ranging from 0 to 500 kHz (with 200 Hz resolution). Here, the number of hidden nodes is selected as 40 to predict the outputs (different fiber orientations). The batch size is selected as 36. The results from an 18-fold cross validation (which ensures that the test data contain every condition from 6 cutting speeds \times 3 FOAs) in terms of the confusion matrix are listed in [Table 2](#). In total, the classification accuracy is around 88 % for different fiber orientation conditions using BD-GRU.

TABLE 2

Confusion matrices for various fiber orientations (BD-GRU vs. BD-LSTM)

		Predicted					Predicted		
BD-GRU		0°	45°	90°	BD-LSTM		0°	45°	90°
Actual	0°	0.9997	0.0000	0.0003	Actual	0°	0.8247	0.1139	0.0615
	45°	0.0481	0.9519	0.0000		45°	0.0156	0.8179	0.1665
	90°	0.0045	0.0000	0.9955		90°	0.0144	0.0024	0.9832

TABLE 3

Testing results for various fiber orientations (BD-GRU vs. BD-LSTM)

		Predicted					Predicted		
		0°	45°	90°			0°	45°	90°
Actual	0°	1.0000	0.0000	0.0000	Actual	0°	0.8333	0.1667	0.0000
	45°	0.3333	0.6667	0.0000		45°	0.0000	0.8333	0.1667
	90°	0.0000	0.0000	1.0000		90°	0.0000	0.0000	1.0000

TABLE 4

Cross validation results for various FOAs using the RF

Confusion Matrix		Predicted		
		0°	45°	90°
Actual	0°	0.8531	0.1259	0.0210
	45°	0.1354	0.7446	0.1200
	90°	0.2047	0.1913	0.6040

Both BD-LSTM and BD-GRU were then applied to test the prediction accuracy on the sequence of each recording. In total, 36 experiment recordings (with various cutting speeds and fiber orientations) were selected in training sets, and 18 recordings were included in each testing set. The classification results are listed in [Table 3](#).

We then compare the results with an earlier investigation on analyzing AE characteristics using random forest (RF) model³³ listed in [Table 4](#). Though the result from the RF model suggests a statistically significant difference between the study cases with $FOA = 0^\circ$ and all others, it could only recognize the difference for $FOA = 45^\circ$ and 90° with around 60 % accuracy. Comparatively, both BD-LSTM and BD-GRU outperform the RF model with consistent accuracy over 87 % toward characterizations of AE signals related to different cutting conditions (FOAs), while BD-GRU consistently achieves higher accuracy for both training and testing.

AE CHARACTERIZATIONS UNDER DIFFERENT CUTTING CONDITIONS

The presented approach was then applied to classify cutting conditions considering both FOAs and cutting speeds for machining NFRP, i.e., $\{y\} = \{(v, FOA) | v \in \{2, 4, 6, 8, 10, 12\}, FOA \in \{0^\circ, 45^\circ, 90^\circ\}\}$. As for implementation details, we select the GRU to construct the BD-GRNN model since it achieves higher classification accuracy (compared with LSTM) toward characterizations of AE temporal-frequency features under different cutting conditions (for the previous case study). The number of nodes N_h is selected as follows:

$$N_h = \frac{\#total\ samples}{\eta \cdot (\#output\ neurons + \#input\ neurons)} \quad (17)$$

where the scaling factor η is set as 2.³⁴ The parameters were selected based on numerical case studies toward multiple settings of the neural network for achieving the highest accuracy. With the actual length given as 140,000 data points, we set the input neurons as 2,499 (frequency bins with 200 Hz resolution for the spectral features at each time step) and the output size as 18 (for 3 FOAs \times 6 cutting speeds). Hence, by selecting a proper scaling number $\eta = 2$ in equation (17), the number of nodes $N_h = \frac{\#total\ samples}{\eta \cdot (\#output\ neurons + \#input\ neurons)} = \frac{140,000}{2 \times 2,517} \approx 28$, and we select the number as 30 in the model. In addition, we also investigate the performance

TABLE 5

Cross validation results (recall/TPR)

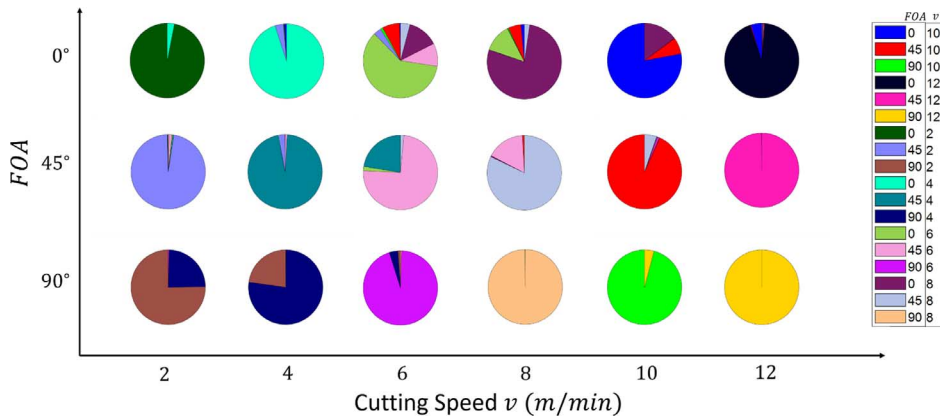
Recall	Cutting Speed, m/min					
FOA	2	4	6	8	10	12
0	0.9912	0.9621	0.8801	0.6169	0.9231	0.9975
45	0.8893	0.8001	0.6611	0.8598	0.7470	0.9902
90	0.7795	0.7064	0.9951	0.9956	0.9804	0.9581

of different activation functions, such as tanh function and ReLU function, on the achieved accuracy. The tanh function has consistent high performance in all cases compared with other functions tested. Based on the guidelines from the literature,³⁵ we selected the batch size as 36, which is the minimal fraction value of the training data size.

Classification results in terms of recall/true positive rate (TPR) values for both cutting speeds and fiber orientations (18 conditions in total) are shown in **Table 5**. Each row represents an *FOA*, and columns are the collection of different cutting speeds. It may be noted that for the higher speed conditions ($v = 10$ and 12 m/min), most cases achieve high TPR (nearly 100 %) for connecting the AE temporal-frequency features to the cutting conditions. However, the classification errors increase when discerning conditions with minor changes in cutting speeds under the same *FOAs*. Details about TPR/recall values given these 18 conditions are listed in Appendix **Table A.2**, where the first column lists the *FOAs*, second column enumerates different cutting speeds (m/min), the diagonal elements are the TPRs, and all the nondiagonal ones represent the false negative rates.

Next, we investigate the classification errors under each condition. **Figure 13** visualizes the detailed classification results (precisions and false positive rate) using pie charts for all 18 conditions. The x axis represents the fiber orientations, and the y axis lists the cutting speeds. The sectors in the pie chart present the portions for true positives as well as false positives under every cutting condition. Each condition (v , *FOA*) is listed in the legend in **figure 13**. Taking the machining condition $FOA = 0^\circ$ and $v = 12$ m/min as one example (represented using the black color in its pie chart (the first row and the sixth column)), the sector under the conditions $FOA = 0^\circ$ and $v = 12$ m/min depicts the precision (ratio of the true positives over sum of true and false positives) and other sectors show the portions of false positives (percent of misclassified data from other conditions). Note that even though such a condition achieves a high accuracy (over 90 % of the TPR), it still has the misclassified portion(s)

FIG. 13 Pie charts showing the precisions of the presented BD-GRNN for AE characterizations under 18 conditions ($FOA \in \{0^\circ, 45^\circ, 90^\circ\}$ and $v \in \{2, 4, 6, 8, 10, 12\}$ (m/min)).



sourced from the condition $FOA = 0^\circ$ and $v = 10$ m/min (colored in blue). Similarly, as for the condition of $FOA = 0^\circ$ and $v = 2$ m/min (the first pie chart in the first row), its false negatives are mostly classified as the conditions with the same orientation ($FOA = 0^\circ$) but the different cutting speed as $v = 4$ m/min (the condition colored in turquoise).

Results from this collection of pie charts may suggest that most false negatives are misclassified in adjacent groups with different cutting speeds but the same FOA . The same cutting mechanism may result in similar temporal-frequency patterns in the AE signals. However, the minor variations (e.g., from 2 to 4 m/min) in cutting speeds may not be significant for changing the AE characteristics. More evidence could also be found in the conditions where $FOA = 90^\circ$. As for the cases under $FOA = 90^\circ$, the relatively low values of both recall and precision ($\sim 77\%$) could be found in the groups in which cutting speeds $v = 2$ and 4 m/min, indicating a large portion ($\sim 20\%$ for each condition) was misclassified between these two conditions with a slight change in cutting speeds.

The reason why AE signatures are more distinguishable under different $FOAs$ is because different $FOAs$ lead to distinct combinations of cutting mechanisms³⁵; under all $FOA = 0^\circ$ conditions, the cutting mechanisms are predominantly the PP matrix removal, with some fibers sliding/shearing along interfacial areas during the material removal; as for the 45° orientation position, the cutting mechanism consists of compression-induced interfacial shearing along the fiber orientation direction, which causes fiber-matrix debonding; for $FOA = 90^\circ$, the fractures that contribute predominantly to fiber pull-out emerge intermittently. Different failure modes during material removal may attribute to different frequency responses of the AE sensor signals. However, classification results also suggest that minor changes in the cutting speed are still less influential on the variations of the resultant temporal-spectral AE features compared with the fiber orientations ($FOAs$).

Despite those groups with comparatively higher false positives (conditions misclassified in adjacent cutting speeds), the presented BD-GRU could achieve an overall $\sim 87\%$ accuracy, while the previously investigated RF could not correctly classify the AE characteristics with respect to the $FOAs$.

Summary and Concluding Remarks

This article presented a framework using a recurrent deep learning approach for real-time monitoring and characterization of sensor signals under transient phase. The temporal-spectral features of AE signals during the NFRP machining processes were selected to test the performance of the presented BD-GRNNs. Admittedly, the feature extraction and selection for the temporal-spectral components remain a major challenge, and investigations into an advanced machine learning approach may be needed to efficiently select energy components within specific frequency band(s). However, the developed GRNNs allow a selection of useful information from the time-frequency features (by training the weights of each neuron) and use gated units to capture the underlying process dynamics on the time-varying spectral information. Thus, ad-hoc feature selection and extraction are avoided. The contributions of this article are listed as follows:

- An illustrative case study is presented to show the performance of the BD-RNN for capturing the transient nature of signals. The results of one (multi)-step forecasting indicate that the GRNN can capture transients (intermittent jumps) between stationary segments and could be used for characterizations for the transient processes.
- The GRNNs (both LSTM and GRU models) are presented for characterizing the AE signals with different transient phase patterns (laminar phases and variations on the modulated time series coefficients). The presented approach achieves around 87 % accuracy, which outperforms other advanced machine learning approaches, such as RF classification, for sequential data classification for characterization of AE signals under different machining conditions. Thus, GRNNs allow real-time process characterizations for machining NFRPs with changes in machining parameters as well as microstructure variations.

For future work, other factors, such as fiber (bundle) distributions and chip formations, need to be considered to characterize AE signals during the machining processes.

ACKNOWLEDGMENTS

Authors would like to thank the National Science Foundation [Civil, Mechanical and Manufacturing Innovation (CMMI #1432914) and Autonomous Experimentation Platform for Accelerating Manufacturing of Advanced Materials (S&AS: INT #1849085)] for supporting the research.

Appendix

TABLE A.1

The 38 experiments of AE recordings with different fiber orientations and tool speeds

Sample No.	Velocity, m/min	Orientation, °	Experiment, Repetition No.
1	2	0	Exp-2
2			Exp-3
3		45	Exp-1
4			Exp-3
5			Exp-4
6	4	90	Exp-1
7		0	Exp-1
8			Exp-2
9			Exp-3
10		45	Exp-1
11	6	90	Exp-1
12		0	Exp-1
13			Exp-2
14			Exp-1
15		45	Exp-2
16	8		
17	90	Exp-1	
18	0	Exp-1	
19		Exp-2	
20		Exp-3	
21	10	45	Exp-1
22			Exp-2
23			Exp-3
24		90	Exp-1
25		0	Exp-1
26	12		
27	Exp-3		
28	45	Exp-1	
29		Exp-2	
30		Exp-3	
31	12	90	Exp-1
32		0	Exp-1
33			Exp-2
34			Exp-3
35		45	Exp-1
36	12		
37	Exp-3		
38	90	Exp-1	

TABLE A.2Confusion matrix for 18 conditions with varying cutting speeds (2, 4, 6, 8, 10, 12 m/min) and *FOA* (0°, 45°, 90°)

<i>FOA</i>	<i>FOA</i>	0	45	90	0	45	90	0	45	90	0	45	90	0	45	90	0	45	90
	Cutting Speed	10	10	10	12	12	12	2	2	2	4	4	4	6	6	6	8	8	8
0	10	0.923	0	0	0.05	0	0	0	0	0	0.009	0	0	0.005	0	0	0.011	0	0
45	10	0.084	0.746	0	0.002	0	0	0	0.001	0	0	0	0	0.111	0	0	0.044	0.007	0
90	10	0	0	0.98	0	0	0	0	0	0	0	0	0	0.014	0	0	0.002	0	0.001
0	12	0	0.001	0	0.997	0	0	0	0	0	0	0	0	0	0	0	0	0	0
45	12	0	0.006	0	0.002	0.99	0	0	0	0	0	0	0	0	0	0	0	0	0
90	12	0	0	0.041	0	0	0.958	0	0	0	0	0	0	0	0	0	0	0	0
0	2	0	0	0	0	0	0	0.991	0.002	0	0.005	0	0	0	0	0	0	0	0
45	2	0	0.002	0	0	0	0	0	0.889	0	0.036	0.023	0	0.048	0	0	0	0	0
90	2	0	0	0	0	0	0	0	0	0.779	0	0	0.209	0	0	0.01	0	0	0
0	4	0	0	0	0	0	0	0.031	0.002	0	0.962	0.001	0	0	0	0	0	0	0
45	4	0	0	0	0	0	0	0	0	0	0	0.8	0	0	0.199	0	0	0	0
90	4	0	0	0	0	0	0	0	0	0.252	0	0	0.706	0	0	0.04	0	0	0
0	6	0	0	0	0.002	0	0	0	0.003	0	0	0	0	0.88	0.016	0	0.096	0	0
45	6	0	0.001	0	0	0	0	0	0.01	0	0	0.007	0	0.145	0.661	0	0.001	0.173	0
90	6	0	0	0	0	0	0	0	0	0.004	0	0	0	0	0	0.995	0	0	0
0	8	0.175	0	0	0.006	0	0	0	0	0	0	0	0	0.195	0	0	0.616	0.005	0
45	8	0	0.042	0	0.001	0	0	0	0.003	0	0	0	0	0.06	0.013	0	0.018	0.859	0
90	8	0	0	0	0	0	0	0	0	0	0	0	0	0	0	0.004	0	0	0.995

References

1. P. Peças, H. Carvalho, H. Salman, and M. Leite, "Natural Fibre Composites and Their Applications: A Review," *Journal of Composites Science* 2, no. 4 (November 2018): 66, <https://doi.org/10.3390/jcs2040066>
2. N. Uddin, ed., *Developments in Fiber-Reinforced Polymer (FRP) Composites for Civil Engineering* (Cambridge, UK: Woodhead Publishing, 2013).
3. L. C. Hollaway and P. R. Head, "Composite Materials and Structures in Civil Engineering," in *Comprehensive Composite Materials* (Amsterdam, the Netherlands: Elsevier, 2000), 489–527.
4. J. George, M. S. Sreekala, and S. Thomas, "A Review on Interface Modification and Characterization of Natural Fiber Reinforced Plastic Composites," *Polymer Engineering and Science* 41, no. 9 (2001): 1471–1485, <https://doi.org/10.1002/pen.10846>
5. A. Valadez-Gonzalez, J. M. Cervantes-Uc, R. Olayo, and P. J. Herrera-Franco, "Effect of Fiber Surface Treatment on the Fiber–Matrix Bond Strength of Natural Fiber Reinforced Composites," *Composites Part B: Engineering* 30, no. 3 (April 1999): 309–320, [https://doi.org/10.1016/S1359-8368\(98\)00054-7](https://doi.org/10.1016/S1359-8368(98)00054-7)
6. D.-E. Lee, I. Hwang, C. M. Valente, J. F. G. Oliveira, and D. A. Dornfeld, "Precision Manufacturing Process Monitoring with Acoustic Emission," *International Journal of Machine Tools and Manufacture* 46, no. 2 (February 2006): 176–188, <https://doi.org/10.1016/j.ijmachtools.2005.04.001>
7. D. A. Dornfeld and E. Kannatey-Asibu, "Acoustic Emission During Orthogonal Metal Cutting," *International Journal of Mechanical Sciences* 22, no. 5 (1980): 285–296, [https://doi.org/10.1016/0020-7403\(80\)90029-6](https://doi.org/10.1016/0020-7403(80)90029-6)
8. J. Barry, G. Byrne, and D. Lennon, "Observations on Chip Formation and Acoustic Emission in Machining Ti–6Al–4V Alloy," *International Journal of Machine Tools and Manufacture* 41, no. 7 (May 2001): 1055–1070, [https://doi.org/10.1016/S0890-6955\(00\)00096-1](https://doi.org/10.1016/S0890-6955(00)00096-1)
9. S. T. S. Bukkapatnam, S. R. T. Kumara, and A. Lakhtakia, "Analysis of Acoustic Emission Signals in Machining," *Journal of Manufacturing Science and Engineering* 121, no. 4 (November 1999): 568–576, <https://doi.org/10.1115/1.2833058>
10. A. Kelly and C. Zweben, eds., *Comprehensive Composite Materials* (Oxford, UK: Pergamon, 2000).
11. Z. Wang, S. T. S. Bukkapatnam, S. R. T. Kumara, Z. Kong, and Z. Katz, "Change Detection in Precision Manufacturing Processes Under Transient Conditions," *CIRP Annals* 63, no. 1 (2014): 449–452, <https://doi.org/10.1016/j.cirp.2014.03.123>
12. D.-C. Chang and S. Bukkapatnam, "Towards Characterizing the Microdynamics of AE Generation in Machining," *Machining Science and Technology* 8, no. 2 (2004): 235–261, <https://doi.org/10.1081/MST-200028743>
13. S. Bukkapatnam and D.-C. Chang, "A Statistical Mechanistic Model of Acoustic Emission Generation in Shear Zone of Machining," *Transactions of NAMRI/SME* 33 (2005): 597–604.
14. F. F. Csikor, C. Motz, D. Weygand, M. Zaiser, and S. Zapperi, "Dislocation Avalanches, Strain Bursts, and the Problem of Plastic Forming at the Micrometer Scale," *Science* 318, no. 5848 (October 2007): 251–254, <https://doi.org/10.1126/science.1143719>
15. G. Hinton, L. Deng, D. Yu, G. E. Dahl, A.-R. Mohamed, N. Jaitly, A. Senior, et al., "Deep Neural Networks for Acoustic Modeling in Speech Recognition: The Shared Views of Four Research Groups," *IEEE Signal Processing Magazine* 29, no. 6 (November 2012): 82–97, <https://doi.org/10.1109/MSP.2012.2205597>
16. R. Trianto, T.-C. Tai, and J.-C. Wang, "Fast-LSTM Acoustic Model for Distant Speech Recognition," in *2018 IEEE International Conference on Consumer Electronics (ICCE)* (Piscataway, NJ: Institute of Electrical and Electronics Engineers, 2018), 1–4.
17. S. V. Kamarthi, S. R. T. Kumara, and P. H. Cohen, "Wavelet Representation of Acoustic Emission in Turning Process," in *Proceedings of the 1995 Artificial Neural Networks in Engineering, ANNIE'95* (Fairfield, NJ: ASME, 1995), 861–866.
18. S. Pittner, S. V. Kamarthi, and Q. Gao, "Wavelet Networks for Sensor Signal Classification in Flank Wear Assessment," *Journal of Intelligent Manufacturing* 9 (August 1998): 315–322, <https://doi.org/10.1023/A:1008970608121>
19. S. Pittner and S. V. Kamarthi, "Feature Extraction from Wavelet Coefficients for Pattern Recognition Tasks," *IEEE Transactions on Pattern Analysis and Machine Intelligence* 21, no. 1 (January 1999): 83–88, <https://doi.org/10.1109/34.745739>
20. T. Mikolov, S. Kombrink, L. Burget, J. Černocký, and S. Khudanpur, "Extensions of Recurrent Neural Network Language Model," in *2011 IEEE International Conference on Acoustics, Speech and Signal Processing (ICASSP)* (Piscataway, NJ: Institute of Electrical and Electronics Engineers, 2011), 5528–5531.
21. H. Sak, A. Senior, and F. Beaufays, "Long Short-Term Memory Recurrent Neural Network Architectures for Large Scale Acoustic Modeling" (paper presentation, 15th Annual Conference of the International Speech Communication Association - INTERSPEECH 2014, Singapore, September 14–18, 2014).
22. A. Graves, A.-R. Mohamed, and G. Hinton, "Speech Recognition with Deep Recurrent Neural Networks," in *2013 IEEE International Conference on Acoustics, Speech and Signal Processing* (Piscataway, NJ: Institute of Electrical and Electronics Engineers, 2013), 6645–6649.
23. S. T. S. Bukkapatnam, S. R. T. Kumara, and A. Lakhtakia, "Fractal Estimation of Flank Wear in Turning," *Journal of Dynamic Systems, Measurement, and Control* 122, no. 1 (March 2000): 89–94, <https://doi.org/10.1115/1.482446>
24. P. Rao, S. Bukkapatnam, O. Beyca, Z. J. Kong, and R. Komanduri, "Real-Time Identification of Incipient Surface Morphology Variations in Ultraprecision Machining Process," *Journal of Manufacturing Science and Engineering* 136, no. 2 (April 2014): 021008, <https://doi.org/10.1115/1.4026210>

25. C. Cheng, Z. Wang, W. Hung, S. T. S. Bukkapatnam, and R. Komanduri, "Ultra-Precision Machining Process Dynamics and Surface Quality Monitoring," *Procedia Manufacturing* 1 (2015): 607–618, <https://doi.org/10.1016/j.promfg.2015.09.044>
26. E. Kannatey-Asibu Jr. and D. A. Dornfeld, "A Study of Tool Wear Using Statistical Analysis of Metal-Cutting Acoustic Emission," *Wear* 76, no. 2 (February 1982): 247–261, [https://doi.org/10.1016/0043-1648\(82\)90009-6](https://doi.org/10.1016/0043-1648(82)90009-6)
27. E. Kannatey-Asibu Jr. and D. A. Dornfeld, "Quantitative Relationships for Acoustic Emission from Orthogonal Metal Cutting," *Journal of Engineering for Industry* 103, no. 3 (August 1981): 330–340, <https://doi.org/10.1115/1.3184493>
28. Z. Wang and S. T. S. Bukkapatnam, "A Dirichlet Process Gaussian State Machine Model for Change Detection in Transient Processes," *Technometrics* 60, no. 3 (May 2018): 373–385, <https://doi.org/10.1080/00401706.2017.1371079>
29. J. Chung, C. Gulcehre, K. Cho, and Y. Bengio, "Empirical Evaluation of Gated Recurrent Neural Networks on Sequence Modeling," *arXiv preprint arXiv:1412.3555*, 2014, <http://web.archive.org/web/20200306190043/https://arxiv.org/abs/1412.3555>
30. A. Hase, M. Wada, T. Koga, and H. Mishina, "The Relationship between Acoustic Emission Signals and Cutting Phenomena in Turning Process," *The International Journal of Advanced Manufacturing Technology* 70, no. 5 (February 2014): 947–955, <https://doi.org/10.1007/s00170-013-5335-9>
31. C. François, "Keras: The Python Deep Learning Library," Keras, <http://web.archive.org/20200117052317/https://keras.io/>
32. T. T. Um, F. M. J. Pfister, D. Pichler, S. Endo, M. Lang, S. Hirche, U. Fietzek, and D. Kulić, "Data Augmentation of Wearable Sensor Data for Parkinson's Disease Monitoring Using Convolutional Neural Networks," *arXiv preprint arXiv:1706.00527*, 2017, <http://web.archive.org/web/20200306191019/https://arxiv.org/abs/1706.00527>
33. Z. Wang, F. Chegdani, N. Yalamarti, B. Takabi, B. Tai, M. E. Mansori, and S. T. S. Bukkapatnam, "Acoustic Emission (AE) Characterization of Natural Fiber Reinforced Plastic (NFRP) Composite Machining Using a Random Forest Machine Learning Model," *Journal of Manufacturing Science and Engineering* 142, no. 3 (January 2020): 031003, <https://doi.org/10.1115/1.4045945>
34. D. Stathakis, "How Many Hidden Layers and Nodes?," *International Journal of Remote Sensing* 30, no. 8 (April 2009): 2133–2147, <https://doi.org/10.1080/01431160802549278>
35. N. S. Keskar, D. Mudigere, J. Nocedal, M. Smelyanskiy, and P. T. P. Tang, "On Large-Batch Training for Deep Learning: Generalization Gap and Sharp Minima," *arXiv preprint arXiv:1609.04836*, 2016, <http://web.archive.org/web/20200306191156/https://arxiv.org/abs/1609.04836>
36. S. Hochreiter and J. Schmidhuber, "Long Short-Term Memory," *Neural Computation* 9, no. 8 (1997): 1735–1780, <https://doi.org/10.1162/neco.1997.9.8.1735>